Applied Surface Science 492 (2019) 219–227

Contents lists available at ScienceDirect

Applied Surface Science

journal homepage: www.elsevier.com/locate/apsusc

Full length article

Covalent bonding of ZnO nanostructures with dispersible carbon nanotubes for self-assembly photocatalytic heterostructures

Weiwei Tie[a,b], Jiaming Jin[a,b], Surjya Sarathi Bhattacharyya[d], Hongwei Yue[a,b], Yan Lei[a,b], Zhi Zheng[a,b], Weiwei He[a,b,*], Seung Hee Lee[c,**]

[a] Key Laboratory of Micro-Nano Materials for Energy Storage and Conversion of Henan Province, School of Advanced Materials and Energy, Institute of Surface Micro and Nanomaterials, Xuchang University, Xuchang, Henan 461000, China
[b] Henan Joint International Research Laboratory of Nanomaterials for Energy and Catalysis, Xuchang University, Xuchang, Henan 461000, China
[c] Applied Materials Institute for BIN Convergence, Department of BIN Fusion Technology and Department of Polymer Nano-Science and Technology, Chonbuk National University, Jeonju, Jeonbuk 54896, South Korea
[d] Asutosh College, 92, Shyamaprasad Mukherjee Road, Kolkata 700 026, West Bengal, India

ARTICLE INFO

Keywords:
Zinc oxide
Carbon nanotube
Photocatalysis
Heterostructures
RhB dyes
Degradation

ABSTRACT

This work demonstrates the fabrication of zinc oxide-carbon nanotube (ZnO/CNT) heterostructures with tunable photocatalytic activity via microstructure modulation. The ZnO/CNT heterostructures are constructed in one-step hydrothermal procedure consisting of in situ anchoring of ZnO nanostructures with dispersible CNTs in an aqueous alkali solution containing bile salts as a dispersant. Observation via scanning (SEM) and transmission (TEM) electron microscopy reveals self-assembled heterostructures of monodispersible CNTs tightly surrounding ZnO nanostructures with multimorphology. The XRD, FT-IR, Raman and XPS analysis confirm that the CNTs were successfully incorporated into the ZnO nanostructures with strong interfacial contact of covalent bonding rather than simple mixing. A series of ZnO/CNT heterostructures, which varies according to their degree of doping with dispersible CNTs, exhibit distinct sunlight-induced photocatalytic activity onto the degradation of Rhodamine B (RhB). The superior photocatalytic performance of ZnO/CNT heterostructures originates from synergistic effects of sufficient interfacial bonding, self-assembly microstructures, and continuous conducting pathways between ZnO nanostructures and CNTs, which acquires better sunlight utilization and more efficient separation of electron-hole pair, confirmed by UV–Visible diffuse reflectance spectra as well as photocurrent and photovoltage analysis. This study also proposes a photocatalytic degradation mechanism of RhB dyes through detection of active species confirmed by electron-spin-resonance analysis.

1. Introduction

Sunlight-induced photocatalytic degradation is a well-studied technology for eliminating the environmental pollutants which have accompanied the rapid development of society [1–3]. Recent photocatalytic advancements have developed various ZnO nanostructures with distinct morphologies and sizes as a promising alternative photocatalyst, which possess a similar energy level and higher absorption efficiency in the range of the solar spectrum compared to conventional TiO_2 [4–6]. However, the wide band gap renders ZnO nanostructures most suitable for absorption in ultraviolet light rather than visible light in the solar spectrum, and their large specific surface area prompts a strong tendency to agglomerate [7,8]. Furthermore, the photocatalytic efficiency and recycling catalytic utilization efficiency of ZnO nanostructures are significantly limited because of the quick recombination of their photoelectron-hole pairs [9,10]. Therefore, improving the photocatalytic and recycling efficiency of ZnO nanostructures is the key to practical photocatalytic applications.

Recent research efforts have focused on ZnO nanostructure-based heterojunctions, which enhance the nanostructures' photocatalytic properties [11–13]. Heterostructures generally consist of two components and possess characteristics of both, having a synergistic effect [14–16]. Among them, CNT-based heterojunctions for photocatalysts are of particular interest due to their unique molecular geometry and the excellent inherent optoelectronic properties of CNTs [12,13]. However, CNT' optoelectronic properties are considerably influenced

* Correspondence to: W. He, Key Laboratory of Micro-Nano Materials for Energy Storage and Conversion of Henan Province, School of Advanced Materials and Energy, Institute of Surface Micro and Nanomaterials, Xuchang University, Xuchang, Henan 461000, China.
** Corresponding author.
E-mail address: lsh1@chonbuk.ac.kr (S.H. Lee).

https://doi.org/10.1016/j.apsusc.2019.06.121
Received 26 March 2019; Received in revised form 1 June 2019; Accepted 12 June 2019
Available online 18 June 2019
0169-4332/

by their dispersion [7,8]. By contrast, monodispersible CNT/ZnO heterojunctions based on self-assembly microstructures can be fabricated to effectively facilitate charge transfer and separation. These materials could be tailored to maximize their photocatalytic degradation abilities due to their continuous conducting pathways and extensive interfacial contact. Various studies have developed new ZnO/CNT heterostructures and their synthesis procedures necessary to achieve them [8,17–19], but little work has focused on self-assembly microstructures between monodispersible CNT and ZnO nanostructures with multimorphology. Therefore, it is of great importance to identify a simple and efficient method to prepare optimal self-assembly heterostructures between multimorphologied ZnO nanostructures and highly dispersed CNT.

In-situ solution synthesis is the simplest and least energy-intensive approach for preparing self-assembly ZnO/CNT heterostructures. This synthesis route allows for easily self-assembly ZnO nanostructures with multimorphology by manipulating experimental conditions such as solvent type, starting materials, and reaction conditions. Furthermore, in-situ solution synthesis can effectively reduce aggregation tendency of ZnO nanostructures in dispersible CNT aqueous solution, which improves light absorption efficiency of ZnO nanostructures and the separation efficiency of the photogenerated electron-hole pairs [19–21].

Herein, we employ a facile, one-step hydrothermal procedure to prepare ZnO/CNT heterostructures with tunable photocatalytic activity. This tunability results from microstructure modulation based on varying degrees of doped dispersible CNTs. Therefore, we can evaluate the crucial role of CNT electron conductivity in the context of photocatalytic activity. We also identify the contribution of self-assembly microstructures of ZnO nanostructures linking with dispersible CNTs to enhanced heterostructure photocatalytic performance via the degradation of RhB dyes under sunlight irradiation. The formation of ZnO/CNT heterostructures and the corresponding interfacial charge-transfer mechanisms are investigated in detail through surface photovoltage, Transient photocurrent, and electron-spin-resonance analysis.

2. Experimental

2.1. Materials

Multi-walled carbon nanotube (CNT) used to prepare CNT-ZnO was supplied by the Chinese Academy of Sciences in Sichuan (China). 98% H_2SO_4, 60% HNO_3, sodium hydroxide (NaOH), $ZnCl_2{\cdot}2H_2O$, and Rhodamine B (RhB) were purchased from China Reagent Company, LTD. The bile salts (BS) used as dispersants for CNT consisted of mixtures of cholic acid and deoxycholic acid sodium salts, which were purchased from Fluka [22]. All chemicals were analytical grade and were used as received without further purification.

2.2. Preparation of f-CNT

Functionalized CNT (f-CNT) were prepared through an acid oxidation process [23]. About 100 mg of CNT powder was mixed with 50 mL of a 3:1 (v/v) mixture of concentrated H_2SO_4 (98%) and HNO_3 (68%) in a 100 mL glass bottle and stirred at 50 °C for 8 h [7]. Following centrifugation at 8000 rpm for 30 min, the supernatant was decanted and filtered through a 0.2 μm anodic alumina membrane (Whatman). The product underwent several more cycles of centrifugation followed by washing with deionized water, until achieving a pH ~ 7. Finally, drying the solution in a vacuum oven at 60 °C yielded CNT powder, hereafter referred to as f-CNT.

2.3. Synthesis of CNT/ZnO heterostructures

CNT/ZnO heterostructures were all synthesized by a hydrothermal method employing the hydrolysis of $ZnCl_2$. In a typical procedure, 0.015 g BS dispersant and a specified amount of f-CNT was dispersed in 15 mL deionized water with sufficient stirring and 30 min of sonication. Then a mixture of 0.1 g $ZnCl_2$ and 0.4 g NaOH was added to the BS-CNT solution, and the resulting mixture was sonicated for 30 min to ensure good dispersion. The homogeneous solution was transferred to a 50 mL Teflon-sealed autoclave and maintained at 150 °C for 6 h. Finally, a series of CNT/ZnO heterostructures were washed with distilled water and ethanol several times to remove unreacted products and were then vacuum-dried at 50 °C for 12 h. The CNT/ZnO heterostructures were designated CNT/ZnO-1, CNT/ZnO-2, and CNT/ZnO-3, corresponding to doped f-CNT masses of 1.0 mg, 2.5 mg, and 5.0 mg, respectively. For comparison, pure ZnO was also prepared using the same procedure without the addition of f-CNT. The purifying and drying procedures for pure ZnO were similar to those described for CNT/ZnO heterostructures.

2.4. Characterization

X-ray diffraction (XRD) patterns of all samples were measured using an X-ray diffractometer (Bruker D8 Advance) with Cu-Kα radiation (λ = 1.5406 Å). The surface morphologies and microstructures of the samples were examined using a scanning electron microscope (SEM, FEI Nova NanoSEM 450) and transmission electron microscope (TEM, Jeol Jem-2100F). Raman spectroscopic analysis was performed using a Perkin Elmer Spectrum-GX and Renishaw in Via Raman spectrometer with a laser excitation of 532 nm. FT-IR spectroscopy was performed using a JASCO FT/IR-460 plus FT-IR spectrometer. A UV–Vis-Infrared spectrophotometer (Agilent Cary-5000) was used to record the UV–vis spectra of various samples. X-ray photoelectron spectroscopy (XPS) of all samples was conducted with an XPS spectrometer (Thermo Escalab 250XI, USA) with Al-Kα radiation (hν = 1486.6 eV). Micromeritics ASAP 2460 nitrogen adsorption apparatus (U.S.) was utilized to investigate the Brunauer-Emmett-Teller (BET) specific surface area (S_{BET}) of the samples by nitrogen adsorption [24]. Surface photovoltage (TPV) spectroscopy was carried out using the standard method as reported by Y. Lei et al. [25] The detected device exhibited typical sandwich structure: Firstly, almost 2 mg powdered samples of ZnO and ZnO/CNT-2 were horizontally tiled onto one indium tin oxide (ITO) glass as bottom substrate; secondly, the other ITO glass placed as top substrate, and mica spacer was used to maintain the suitable gap between the two electrodes. The laser pulses (355 nm with a pulse width of 4 ns) was supplied by the third-harmonic Nd: YAG laser (Quantel Brilliant Eazy: BRILEZ/IR-10), and TPV signals were recorded utilizing a digital oscilloscope with frequency of 500 MHz (TDS 3054C, Tektronix).

Photocurrent measurements were taken using a CHI 660 potentiostat (CH Instruments) in a standard three-electrode system immersed in a 0.1 M KCl solution under simulated sunlight irradiation of approximately 100 mW/cm^2 [26]. A platinum electrode and Ag/AgCl electrode were used as the counter and reference electrodes, respectively. The working electrode was prepared by the following process: A homogeneous mixture of pure ZnO or ZnO/CNT-2 hybrid (4.5 mg) and polyvinylidene fluoride (1 mg) in *N*-methyl pyrrolidone (1 mL) was prepared by sonicating for 15 min, and then the electrode film was formed with 1 cm x1.5 cm effective area by drop casting the resultant mixture onto ITO glass and drying at 60 °C under vacuum for 2 h.

2.5. Photocatalytic activity

To evaluate the photocatalytic performance of the heterostructures, the degradation of Rhodamine B (10 mg/L) in water was measured under sunlight irradiation. Powdered catalyst samples of 10 mg were dispersed in 50 mL Rhodamine B aqueous solution (10 mg/L) and the suspension was stirred under dark ambient conditions for 40 min to reach adsorption-desorption equilibrium. With continuous stirring, the suspension was exposed to simulated solar irradiation emitted by a 500 W Xenon lamp. Aqueous solution was withdrawn regularly from the suspension and the catalysts were separated via centrifugation.

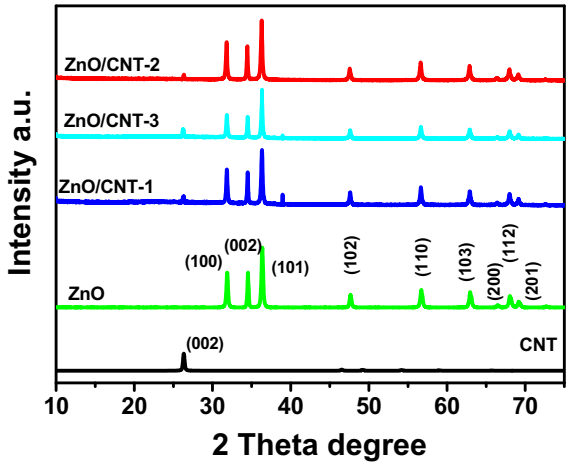

Fig. 1. XRD pattern of all samples.

After removing the catalysts, the remaining transparent supernatant was analyzed by UV/Vis absorbance spectroscopy. The degradation process was monitored by measuring the absorption of Rhodamine B at 554 nm. The degradation efficiency was calculated according to $\eta = C_t/C_0$ [8,19]. The photocatalytic degradation of Rhodamine B was expressed using the apparent pseudo-first-order kinetics equation according to the Langmuir-Hinshelwood kinetics model, $\kappa = \ln (C_t/C_0)$ [19], where κ was the apparent pseudo-first-order rate constant, C_0 was the RhB dye concentration in the original aqueous solution, and C_t was the RhB dye concentration at sunlight irradiation time (t).

3. Results and discussion

XRD analysis is performed to explore the phase and crystal structure of all samples. Fig. 1 shows the XRD patterns for pure ZnO, f-CNT, ZnO/CNT-1, ZnO/CNT-2, and ZnO/CNT-3. Pure f-CNT exhibits a broad characteristic diffraction peak at approximately $2\theta = 26.2°$, corresponding to the (002) plane of the graphene structure comprising the CNT surface [19]. Pure ZnO is characterized by diffraction peaks at 31.9°, 34.6°, 36.4°, 47.7°, 56.7°, 62.9°, 66.3°, 68.0°, and 69.2°, which are attributed to the ZnO's crystal planes at (100), (002), (101), (102), (110), (103), (200), (112), and (201), respectively [27]. These diffraction peaks are consistent with the standard peak values reported for ZnO, and there are no additional miscellaneous peaks, indicating that the ZnO nanostructures are highly pure. In contrast to the XRD pattern of pure CNT or ZnO, CNT/ZnO heterostructures possess virtually the same peaks as pure ZnO, as well as a new diffraction peak at $2\theta = 26.2°$ corresponding to the characteristic (002) crystalline planes of CNT. Therefore, the XRD analysis provides strong evidence that all of the CNT/ZnO heterostructures are composed of both ZnO crystals and CNTs. The average crystalline size of the CNT-hybridized ZnO heterostructures can be calculated with Scherrer's formula: $d = k\lambda/\beta\cos\theta$, where d is the averaged crystal size, $k = 0.9$, λ is the X-ray radiation wavelength, β is the full width at half maximum of diffracted peak, and θ is the diffraction angle [8]. The formula yields an average crystalline size of approximately 35 nm, which is in agreement with the following SEM and TEM analysis. Considering the superior photocatalytic performance of ZnO/CNT-2 during a series of photo catalysis, we will pay more attention to this kind of material for further structure characterization and property evaluation in the following sections.

SEM images are captured to observe the micromorphology of ZnO/CNT-2 heterostructures shown in Fig. 2. The ZnO crystals show self-assembly nanostructures with multimorphology including nanorods and nanoplates. It is found f-CNTs with width of approximately 20 nm and lengths of approximately 1 μm are monodispersed into self-assembly ZnO nanostructures. The CNTs closely contact with the surface of ZnO nanostructures, bestowing a strong interaction between the two components. This interaction is robust enough to resist separation of ZnO and CNT, even after repetitive washing and ultrasonication. To further investigate the microstructure of the ZnO/CNT-2 heterostructures, TEM imaging is performed in Fig. 3. Fig. 3(a,b) depicts dispersible CNTs with diameter of about 20 nm are in tight contact with multimorphologied ZnO nanostructures for optimal self-assembly microstructures, coalescing into a ZnO/CNT heterostructure [19]. These results are in agreement with SEM analysis and further reinforce that ZnO nanostructures and CNT combine into well-formed heterostructures. Elemental mapping of TEM images (Fig. 3c) reveals that carbon is distributed in networks (Fig. 2d), while oxygen and zinc are clustered together in different configurations in Fig. 3(e,f). Therefore, elemental mapping confirms the successful fabrication of ZnO/CNT heteroarchitectures and is consistent with SEM and TEM observations.

Raman spectroscopy was used to study the incorporation of CNT into ZnO nanostructures. Fig. 4 shows the Raman spectra of pure f-CNT, pure ZnO, and ZnO/CNT-2 heterostructures. The ZnO possess characteristic peaks at 325, 380, and 434 cm^{-1}, respectively, corresponding to the $2E_2$ (M), A_1 (TO), and E_2 (high) vibration modes of ZnO's crystal structure [8,19]. Pure f-CNT displays characteristic signals of the D band (vibration of defects in a single graphene layer) and the G band (bond stretching of sp^2-hybridized carbon atoms), which appear at 1335 and 1584 cm^{-1}, respectively. ZnO/CNT heterostructures display Raman signals including the peaks of both ZnO and CNT. The calculated intensity ratio (I_D/I_G) is approximately 0.96 for pure f-CNT and 0.90 for ZnO/CNT heterostructures. The decrease in I_D/I_G value observed in the heterostructures compared to the pure f-CNT indicates fewer defects and disorders in the graphene-like surface of ZnO/CNT-2 heterostructures, suggesting the formation of more sp^2 carbon during the in-situ reaction between ZnO and CNT [28,29]. Additionally, the G band shift from 1570 cm^{-1} for pure f-CNT to 1578 cm^{-1} for ZnO/CNT heterostructures suggests that a strong interaction occurs between CNT and ZnO in ZnO/CNT heterostructures, namely, indicating charge transfer occurring between the components through chemical bonding [7,8].

FT-IR and XPS analyses yield more detailed information about the chemical structure and atomic bonding states of pure ZnO and ZnO/CNT heterostructures. Fig. 5 presents the FT-IR spectra of the ZnO/CNT-2 compared to those of pure ZnO and f-CNT. The f-CNT possesses a characteristic band at 1625 cm^{-1} due to the C=C stretching vibration of graphene, while the ZnO spectrum bears a peak at 515 cm^{-1} corresponding to the transverse optical stretching modes of ZnO [29]. Notably, both of these pure components' peaks appear in the FT-IR spectrum of the ZnO/CNT heterostructures, indicating the presence of C=C and Zn-O-Zn bond stretching contributed by CNT and ZnO in the heterostructures, respectively [30]. These results clearly reveal that ZnO nanostructures successfully hybridize with CNTs, with the Zn-O-Zn bond stretching in ZnO/CNT-2, indicating the Zn-O-Zn antisymmetric and symmetric vibrations in the ZnO/CNT heteroarchitectures.

To further confirm the chemical bonding kind between ZnO and CNT in ZnO/CNT composite, the high-resolution XPS spectra have been probed in Fig. 6. The deconvoluted XPS C1s spectrum for ZnO/CNT-2 shown in Fig. 6a exhibits five peaks fitted at binding energies of 283.48, 284.58, 285.18, 286.08, and 288.48 eV, corresponding to carbon atoms in different functional groups. The peaks at approximately 284.6 and 285.1 eV are contributions of the C=C (sp^2) and C−C (sp^3) bonds, respectively [21]. The peak at about 286.1 eV is attributed to C-OH bonds, while the peak at 288.54 eV is due to C−OOH bonds [31]. The C 1 s spectrum of the CNT-hybridized ZnO heterostructures does not possess the C 1 s peak characteristic of Zn−C bonding at 281 eV, but a new peak detected at around 283.5 eV can be attributed to C−O−Zn bonding [31]. Fig. 6b demonstrates that the binding energies of Zn $2p_{3/2}$ and $2p_{1/2}$ are centered at 1021.31 and 1044.36 eV, respectively, in agreement with those of pure ZnO [31]. The small shift in the binding energy of Zn 2p 3/2 (1021.4 eV) in the ZnO/CNT compared to that pure

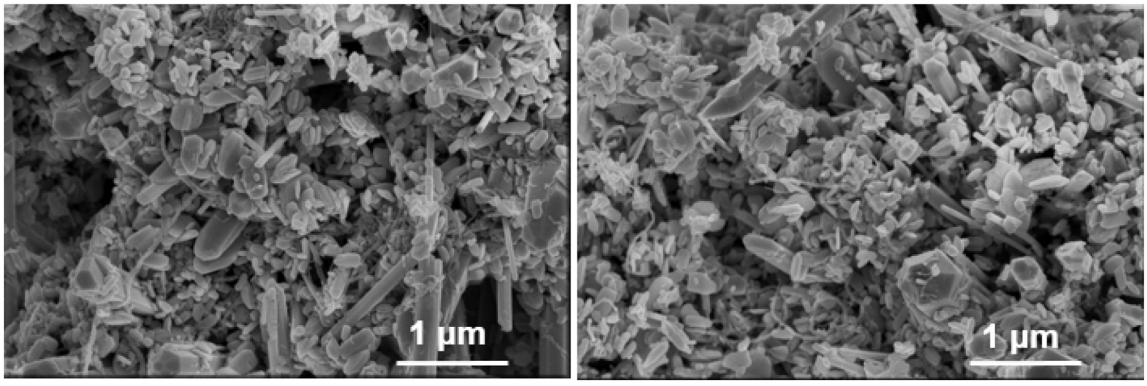

Fig. 2. Scanning electron micrograph of ZnO/CNT-2 heterostructures.

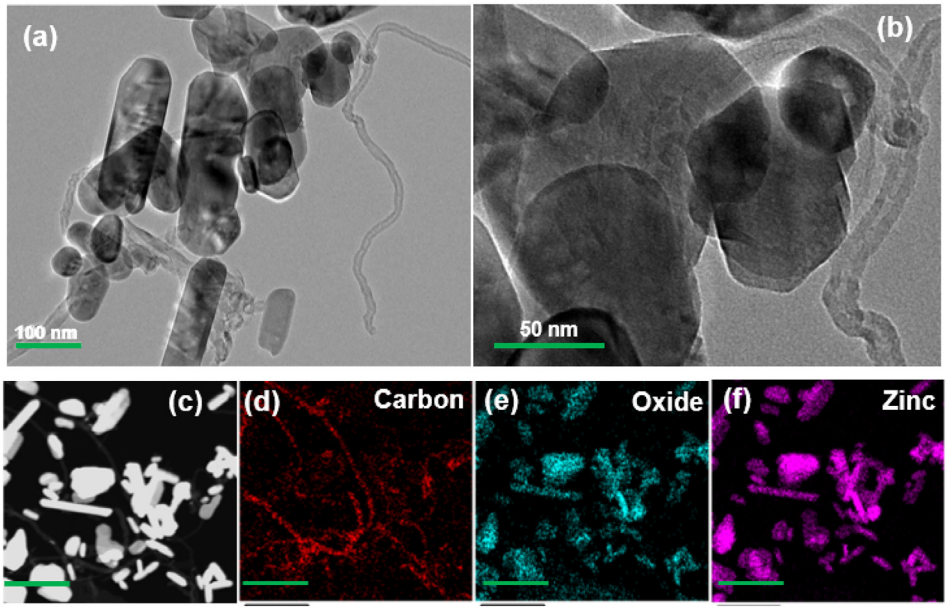

Fig. 3. TEM images of ZnO/CNT-2 heterostructures (a, b) and EDS mapping (c) results of C, O and Zn elements (d–f). The scale bar is 500 nm.

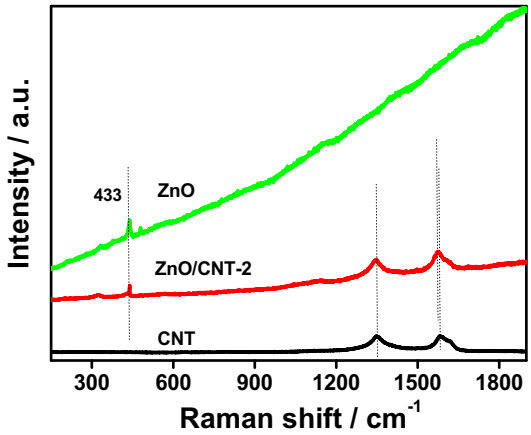

Fig. 4. Raman spectra of pure ZnO, pure CNT, and ZnO/CNT-2 heterostructures.

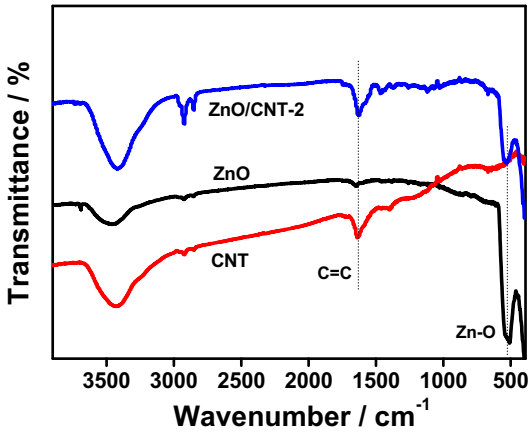

Fig. 5. FT-IR spectra of pure ZnO, pure CNT, and ZnO/CNT-2 heterostructures.

ZnO (1021.2 eV), - indicates chemical C—Zn bond maybe very weak or not formed during the association of ZnO with CNT in our present system [31]. These results suggest that the chemical interaction between ZnO and CNT in our present system is strong, which results from the formed chemical C—O—Zn bond rather than C—Zn bond, which may preserve chemical stability and promote electronic interaction in CNT-hybridized ZnO heterostructures.

UV–vis diffuse reflectance spectra (UV–vis DRS) is utilized to estimate their optical properties of the ZnO/CNT heterostructures and pure ZnO. The UV–vis diffuse reflectance spectra of both pure ZnO and ZnO/CNT heterostructures depicted in Fig. 7a displays intense absorption in

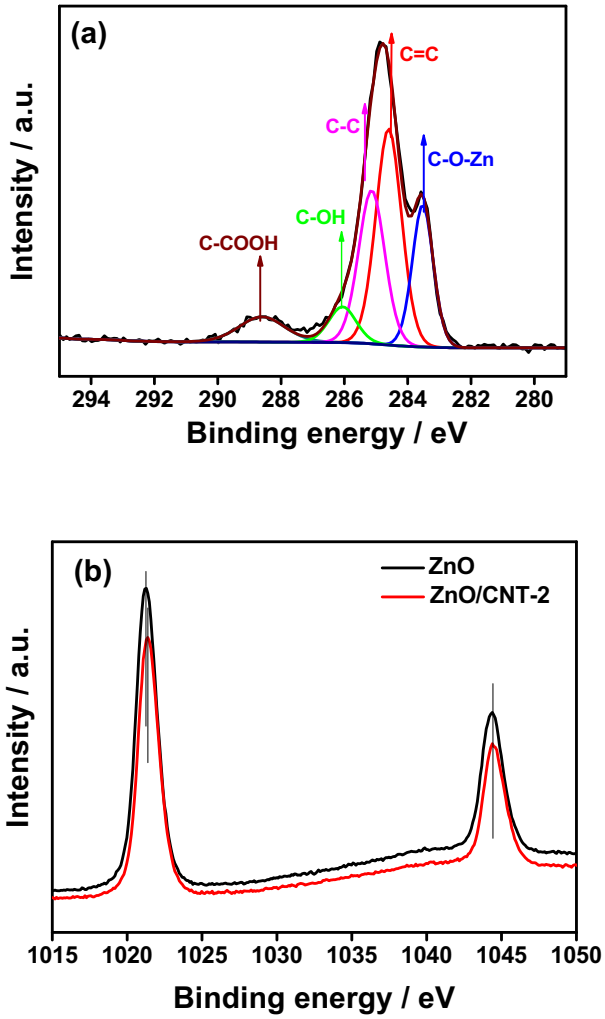

Fig. 6. XPS C1s of ZnO/CNT-2 (a) and Zn 2p spectra (b) of pure ZnO and ZnO/CNT-2 heterostructures.

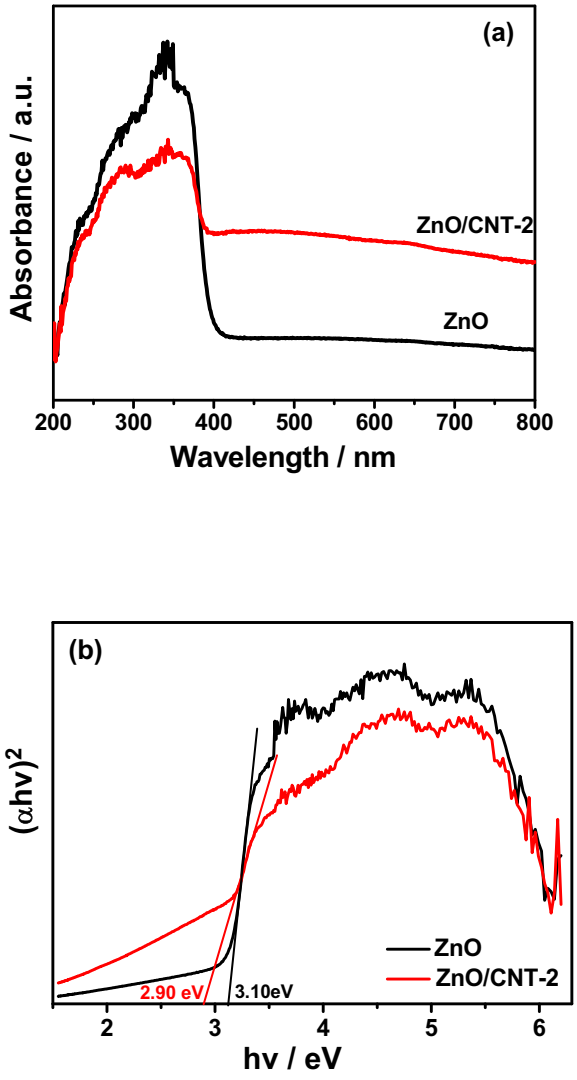

Fig. 7. UV–vis DRS spectra (a) and Energy (hν) vs $(\alpha h\nu)^2$ curves (b) of pure ZnO and ZnO/CNT-2 heterostructures.

the UV region around 350 nm originating from the intrinsic band-edge absorption of ZnO nanostructures [29]. Compared to pure ZnO, ZnO/CNT-2 heterostructure exhibits much stronger absorbance of visible light at wavelengths longer than 400 nm due to the presence of CNTs. This increased visible light absorption is in accordance with the white-to-gray color change observed in pure ZnO sample, which should have important implications regarding their photocatalytic capability, especially under sunlight irradiation. Furthermore, we have calculated the band gap energy of these semiconductors from the curve of $(\alpha h\nu)^2$ versus energy by intercepting the extrapolation of the plots to the x axis using the following equation: $\alpha h\nu = A(h\nu - Eg)^2$ [19]. The calculated *Eg* of ZnO/CNT-2 heterostructures shown in Fig. 7b is approximately 2.90 eV, apparently smaller than that of pure ZnO (3.10 eV). The narrowing in band gap of CNT hybridized ZnO heterostructure makes it harvest visible light easily and then efficiently facilitates photocatalytic activity onto organic dyes, mainly attributing to the chemical bonding between ZnO and CNT due to the formed Zn-O-C bond at the interface confirmed by abovementioned XPS and Raman analysis.

The effect of CNT on the BET surface areas and pore structures of pure ZnO and ZnO/CNT heterostructures have been investigated using nitrogen adsorption-desorption experiments shown in Table 1. Compared to pure ZnO, the BET surface area (S_{BET}) of ZnO/CNT-2 heterostructures increases with adding of CNT, from 10.8 ± 0.1 to 11.7 ± 0.1 m^2/g. This is probably attributed to the low amount of CNT added into the composite. Nitrogen adsorption-desorption isotherms

Table 1
Effect of CNT on the BET surface areas and pore structures of pure ZnO and ZnO/CNT-2 heterostructures.

Samples	BET surface area (m^2/g)	Pore size (nm)	Pore volume (cm^3/g)
ZnO	10.8033	5.04682	0.053
ZnO/CNT-2	11.6643	6.46898	0.041

and the corresponding curves of the pore size distribution (inset) for pure ZnO and ZnO/CNT heterostructures have been shown in Fig. 8. Based on the Brunauer-Dening-Dening-Teller (BDDT) classification, both of pure ZnO and ZnO/CNT-2 are isotherms of type IV, suggesting the presence of mesopores [24]. From the pore diameter distribution shown in the inset curves in Fig. 8, ZnO/CNT-2 composite displays similar mesopores structures but the increased peak pore diameter of around 6 nm compared to that of pure ZnO. The improvement of specific surface area in ZnO/CNT-2 composite provides possibility to increase the surface active sites and makes charge carriers transport as well as adopt and deposit of the degradable dye molecules easier during the photocatalytic process, which is beneficial for superior photocatalytic performance in ZnO/CNT-2 composite.

The photocatalytic properties of pure ZnO and ZnO/CNT heterostructures are evaluated via monitoring the degradation of RhB aqueous

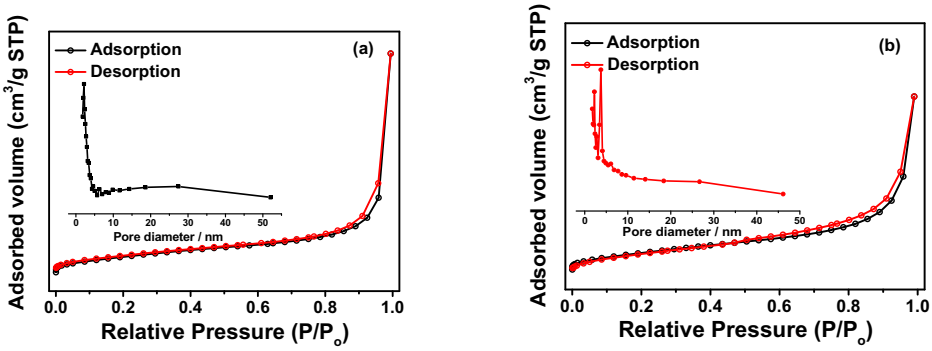

Fig. 8. Nitrogen adsorption-desorption isotherms and pore size distribution curves (inset) of ZnO (a) and ZnO/CNT-2 heterostructures (b).

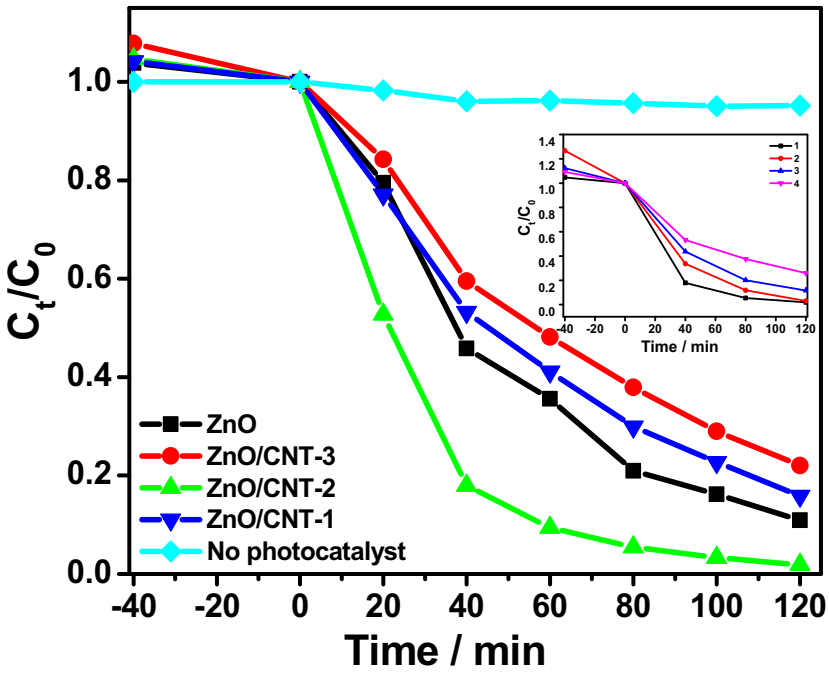

Fig. 9. Photocatalytic degradation of Rhd B with different photocatalysts and photostability curves (inset) under sunlight irradiation.

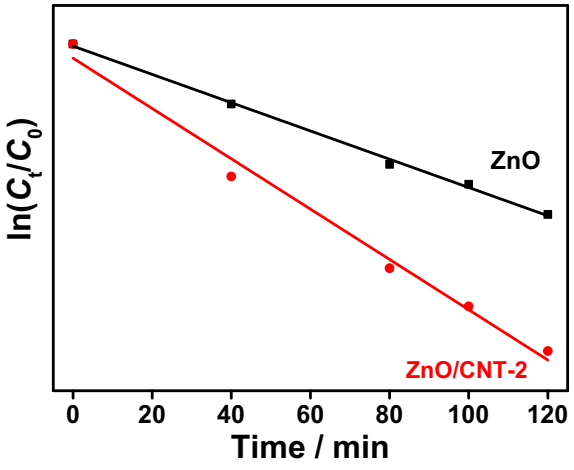

Fig. 10. Kinetics of the photocatalytic degradation of Rhd B with pure ZnO and ZnO/CNT-2 heterostructures under sunlight irradiation.

solution under simulated sunlight irradiation. Fig. 9 shows the catalytic degradation efficiency of pure ZnO as well as ZnO/CNT-1, ZnO/CNT-2, and ZnO/CNT-3 heterostructures. In controlled experiments, less than 1% of RhB is decomposed after 2 h sunlight irradiation without catalyst loading. With photocatalyst, the complete elimination of RhB from solution containing ZnO/CNT-2 heterostructures is achieved after 2 h simulated sunlight irradiation. The RhB solution undergoes a complete color change from deep red to colorless, however, only 68% of which is attributable to pure ZnO within the specified reaction time. Additionally, a series of ZnO/CNT heterostructures with different CNT incorporation remarkably produce different degradation effect, in which the ZnO/CNT-2 with moderate CNT adding has highest catalytic performance due to formed effective conductive pathway of dispersed CNTs in hybrid, confirmed by the abovementioned SEM and TEM observations, and where ZnO/CNT-1 or ZnO/CNT-3 with less or more CNT adding all result in undesirable catalytic effect comparing with pure ZnO without effective conductive pathway. These results clearly indicate incorporating CNTs into heterostructures yielding effective conductive pathways apparently accelerates the degradation process. Kinetic photocatalytic activities are summarized in Fig. 10, which show the variation in ln (C_t/C_0) as a function of irradiation time for pure ZnO and a ZnO/CNT heterostructures. The rate constant k is calculated from the plots of $ln(C_t/C_0)$ vs irradiation time for each material, yielding 0.0184 for ZnO and 0.0327 min^{-1} for the ZnO/CNT heterostructures. This provides clear evidence that CNT introduction into the ZnO material apparently induces a synergistic effect on RhB removal. The

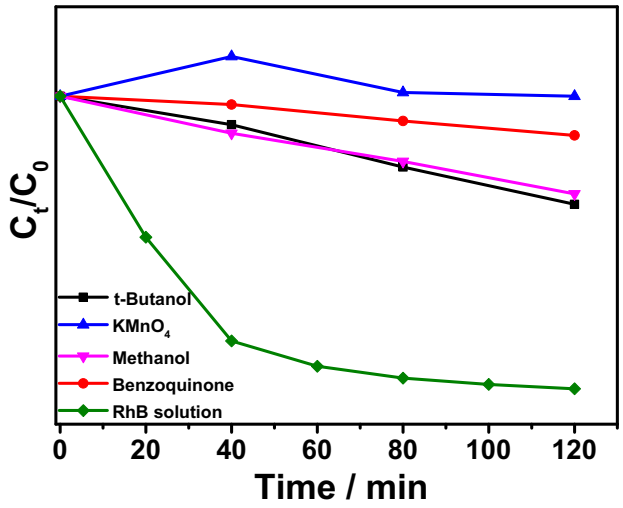

Fig. 11. Photodegradation dynamics of RhB in the presence of ZnO/CNT-2 heterostructures with and without addition of radical scavenger.

photocatalytic stability of ZnO/CNT-2 has been further investigated as the inset curves in Fig. 8. It is found that the decomposition of RhB dye with ZnO/CNT with three repeating recycle are around 97%, 89% and 75%. The decrease of photocatalytic stability of ZnO/CNT onto dyes mainly results from the less formed heterostructures due to small amount of adding of CNTs into ZnO/CNT heterostructures.

The formation of ROS such as hydroxyl radicals (·OH) and superoxide radicals (O_2^-·) under photocatalytic conditions, as well as their role in the Rhd B dye degradation process, is indirectly investigated with appropriate quenchers for these species. Fig. 11 shows photodegradation dynamics of RhB in the presence of ZnO/CNT heterostructures with addition of t-butanol, methanol, potassium permanganate and benzoquinone additives, as well as no additives. Prior to photocatalytic experiments, the catalyst-containing dye solution is kept in dark conditions for 40 min to attain RhB-catalyst adsorption-desorption equilibrium. In the controlled photocatalytic experiments depicted in Fig. 11, a hydroxyl radical scavenger (t-butanol), or superoxide radical scavenger (benzoquinone) or potassium permanganate or methanol for photogenerated electrons or holes scavenger is added to the respective Rhd B dye solutions [32]. T-butanol or methanol clearly decrease the degradation efficiency of Rh B dye but do not prevent degradation entirely, while potassium permanganate or benzoquinone almost completely inhibits RhB degradation. Considering the short lifetime of photogenerated electrons or holes reacted with O_2 or H_2O during the photocatalytic process, these results indicate that O^{2-}· and ·OH^- radicals play an important role in the photocatalytic degradation. ESR (electron spin resonance) spin trapping (with DMPO) is employed to monitor the reactive oxygen species generated. Fig. 12 shows that signals for both DMPO-·OH and DMPO-O_2^-· are clearly observed when pure ZnO or ZnO/CNT suspension is photoirradiated, suggesting the oxidation of both radicals may be involved in the photocatalytic process. However, both signal strength of ·OH^- and O_2^-· in ZnO/CNT composite is obviously higher than that in pure ZnO, suggesting the number of reactive oxidative species involved in the photocatalytic process are much higher in ZnO/CNT-2 than that in pure ZnO. This further confirms that different intensity of reactive oxidative species involved in the photocatalytic process detected in pure ZnO and ZnO/CNT-2 confirmed by the ESR measurement greatly improves their different photocatalytic activity.

Surface photovoltage (SPV) and transient photocurrent (SPC) techniques can be used to evaluate the dynamic generation, transfer and separation characteristics of photogenerated carrier. Fig. 13 shows the SPV spectra for ZnO and ZnO/CNT heterostructures on a logarithmic timescale. Pure ZnO - emit a relatively weak photovoltage signal, but a

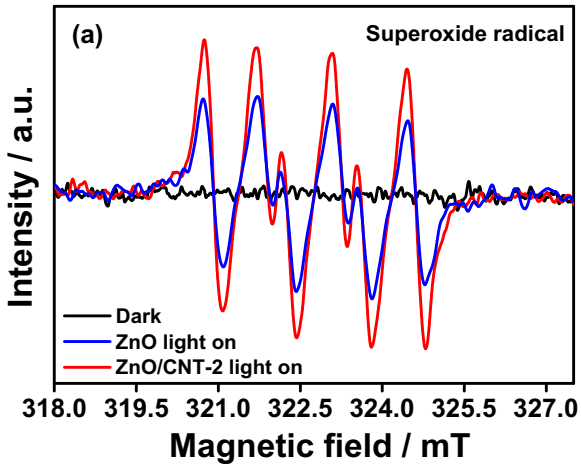

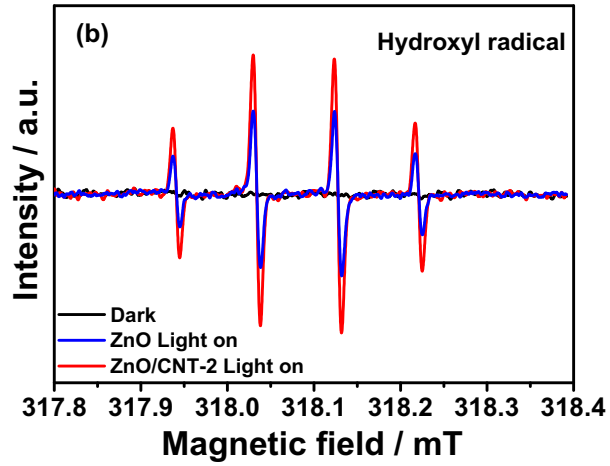

Fig. 12. Electron-spin-resonance spectra of ZnO and ZnO/CNT-2 heterostructures.

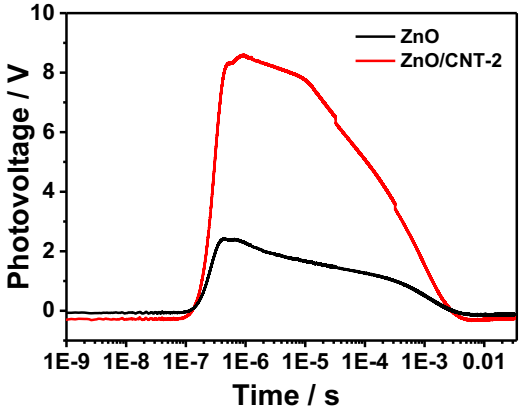

Fig. 13. Surface photovoltage spectra of ZnO and ZnO/CNT-2 heterostructures.

much stronger photovoltage signal is produced by the ZnO/CNT-2 heterostructure. Additionally, the SPV response of the ZnO/CNT-2 heterostructure immediately increases to reach a maximum at a time shorter than 10^{-6} s, while the corresponding maximum value of pure ZnO is much lower. The effective separation of photogenerated charges in ZnO/CNT-2 heterostructure is mainly attributed to the interfacial

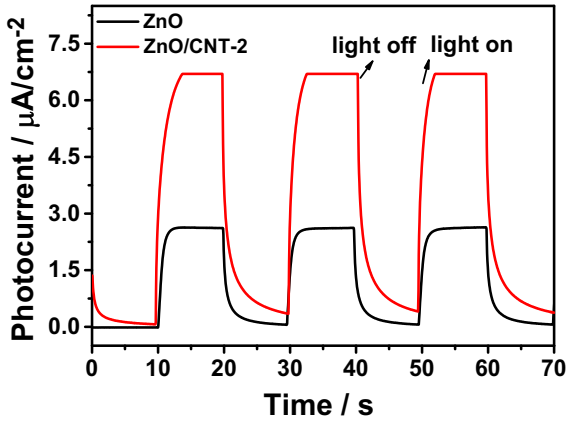

Fig. 14. Photoelectric current spectra of ZnO and ZnO/CNT-2 heterostructures.

electric field induced contribution between ZnO and the CNTs [33]. Furthermore, the SPV signal decreases much slower in the time scale ranging from 10^{-6} s to 10^{-2} s due to the relatively reduced recombination process of photogenerated charges. Overall, a more delayed SPV response results from a lower recombination rate of the photogenerated charges. Therefore, prepared ZnO/CNT heterostructures can effectively prolong the lifetime of the holes, granting the holes more time to participate in the photocatalytic oxidation reaction.

Fig. 14 illustrates the transient photocurrents (TPC) of pure ZnO and ZnO/CNT heterostructures. The pure ZnO exhibits pronounced photocurrent, displaying semiconducting characteristics. As expected, the photo response generated is much higher at the ZnO/CNT heterostructure electrode than that at the ZnO electrode. The photocurrent at the electrode of ZnO/CNT heterostructures is as high as 6.7 μA cm^{-2} under sunlight irradiation, compared to a photocurrent as low as 2.6 μA cm^{-2} at the electrode made of pure ZnO under the same conditions. Due to covalent linking and the compact contact between ZnO and CNT, ZnO/CNT-2 heterostructure displays a current density approximately 2.6 times higher than that of pure ZnO. The microstructure allows for the transfer of photoexcited electrons between ZnO and CNT, as well as effective transfer further to the surface of heterostructures. This transfer occurs even though sunlight irradiation has a lower energy than the band gap energy of ZnO. At the nanohybrid/electrolyte interface, photogenerated holes normally react with OH^- ions, and the electrons are assembled at the electrode to generate photocurrent [34]. The photocurrent response is reproducible throughout repeated light on/off cycles, suggesting efficient charge separation and collection.

The proposed mechanism for the photocatalyic degradation of the ZnO/CNT heterostructures is schematically illustrated in Fig. 15. Photogenerated electrons originating from the excited dye* and the ZnO valence band of ZnO can be excited by sunlight irradiation and transferred to the ZnO conduction band, thus forming electron-hole pairs [35]. These electrons are quickly transferred to the CNT surface and efficiently separated due to continuous conducting pathways and sufficient interfacial contact during self-assembly microstructure of multimorphologied ZnO nanostructures with monodispersible CNT, resulting in a direct and short reaction path, which enhances the heterostructures' photocatalytic activity, confirmed by the SPV and TPC measurements. The electrons captured by the CNTs could react with O_2 to form $O_2^-\cdot$, while the holes in ZnO react with H_2O generate ·OH radicals. Ultimately, the highly reactive ·OH and $O_2^-\cdot$ species decompose the RhB dye into smaller species including carbon dioxide and other inorganic compounds.

4. Conclusion

Self-assembled ZnO/CNT heterostructures consisting of ZnO nanostructures covalently linked to dispersible CNTs are synthesized using a facile one-step hydrothermal procedure. The heterostructures exhibit improved photocatalytic reactivity under sunlight irradiation compared to their pure components. They also demonstrate excellent visible light absorption, which can be harnessed to drive photochemical degradation. The photocatalytic performance of the heterostructures depends on the associated amount of CNT in contact with ZnO with formed effective conductive pathways. The self-assembly ZnO/CNT heterostructures with moderate CNT loading exhibits the highest photocatalytic activity, with a rate constant of 0.0327 min^{-1} and the ability to completely degrade Rhodamine B within 2 h. Photochemical characterization of the ZnO/CNT heterostructures confirmed that the origins of sunlight-induced photocatalytic activity are continuous conducting pathways, sufficient interfacial combination, and strong chemical bonding between ZnO and CNT. The synergistic effect combining these factors facilitates the separation of photoinduced electron-hole pairs and inhibits their recombination, thus increasing photocatalytic efficiency. The facile one-step synthesis offers new insight into the construction of CNT-hybridized ZnO nanostructures to achieve tunable photoactivity. Self-assembly microstructures between dispersible CNT and multimorphologied ZnO heterostructures, as well as the doped monodisperse CNT's high performance as a sunlight-responsive catalyst, contribute to the hybridized heterostructures' outstanding potential for photocatalytic degradation. Therefore, the techniques and concepts described herein show great promise for applications involving photocatalytic degradation of organic compounds, such as environmental pollution cleanup.

Acknowledgments

This research was supported by the National Natural Science Foundation of China (61605167 and 11804289), China; the Program for Innovative Research Team (in Science and Technology) in University of Henan Province (19IRTSTHN026), China; the Key Scientific Research Project of Universities and Colleges in Henan Province (17A430028), China; the Plan for Scientific Innovation Talent of Henan Province (174100510014), China; the Outstanding Young

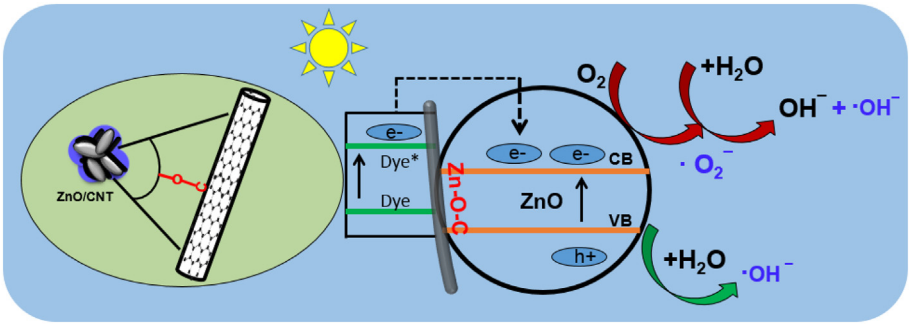

Fig. 15. Photocatalytic mechanism of ZnO/CNT-2 heterostructures under sunlight irradiation.

Backbone Teacher Funding Project of Xuchang University, China; and the Science and Technology Bureau of Xuchang, China.

References

[1] M. Han, S.J. Zhu, S.Y. Lu, Y.B. Song, B. Yang, Recent advances in photocatalysis for environmental applications, J. Environ. Chem. Engineer. Nano Today 19 (2018) 201–218.

[2] C.B. Ong, L.Y. Ng, A.W. Mohammad, A review of ZnO nanoparticles as solar photocatalysts: synthesis, mechanisms and applications, Renew. Sust. Energ. Rev. 81 (2018) 536–551.

[3] D. Chaudhary, S. Singh, V.D. Vankar, N. Khare, J. Photochem. Photobiol. A Chem. 351 (2018) 154–161.

[4] M.G. Wang, J. Han, Y.M. Hu, R. Guo, Mesoporous C, N-codoped TiO_2 hybrid shells with enhanced visible light photocatalytic performance, RSC Adv. 7 (2017) 15513–15520.

[5] Y. Li, W.Q. Cui, L. Liu, R.L. Zong, W.Q. Yao, Y.H. Liang, Y.F. Zhu, Removal of Cr(VI) by 3D TiO_2-graphene hydrogel via adsorption enriched with photocatalytic reduction, Appl. Catal. B Environ. 199 (2016) 412–423.

[6] M.J. Limo, R. Ramasamy, C.C. Perry, ZnO binding peptides: smart versatile tools for controlled modification of ZnO growth mechanism and morphology, Chem. Mater. 27 (2015) 1950–1960.

[7] W.W. Tie, S.S. Bhattacharyya, Y.G. Zhang, Z. Zheng, T.H. Lee, S.W. Lee, T.H. Kim, Y.H. Lee, S.H. Lee, Field-induced stretching and dynamic reorientation of functionalized multiwalled carbon nanotube aggregates in nematic liquid crystals, Carbon 96 (2016) 548–556.

[8] W.W. Tie, Z. Zheng, C. Xu, Z. Zheng, S.S. Bhattacharyya, W.W. He, S.H. Lee, Facile synthesis of carbon nanotubes covalently modified with ZnO nanorods for enhanced photodecomposition of dyes, J. Colloid and Interface Sci. 537 (2019) 652–660.

[9] W.W. He, H.-K. Kim, W.G. Wamer, D. Melka, J.H. Callahan, J.-J. Yin, Photogenerated charge carriers and reactive oxygen species in ZnO/au hybrid nanostructures with enhanced photocatalytic and antibacterial activity, J. Am. Chem. Soc. 136 (2014) 750–757.

[10] W.W. He, H.H. Wu, W.G. Wamer, H.-K. Kim, J.W. Zheng, H.M. Jia, Z. Zheng, J.-J. Yin, Unraveling the enhanced photocatalytic activity and phototoxicity of ZnO/metal hybrid nanostructures from generation of reactive oxygen species and charge carriers, ACS Appl. Mater. Interfaces 6 (2014) 15527–15535.

[11] S. Dong, J. Feng, M. Fan, Y. PI, L. Hu, X. Han, M. Liu, J. Sun, Recent developments in heterogeneous photocatalytic water treatment using visible light-responsive photocatalysts: a review, RSC Adv. 5 (2015) 14610–14630.

[12] S. Wang, B.C. Zhu, M.J. Liu, L.Y. Zhang, J.G. Yu, M.H. Zhou, Direct Z-Scheme ZnO/CdS Hierarchical Photocatalyst for Enhanced Photocatalytic H_2-Production Activity, vol. 243, (2019), pp. 19–26.

[13] P. Zhou, J.G. Yu, M.J. Saint, All-solid-state z-scheme photocatalytic systems, Adv. Mater. 26 (2014) 4920–4935.

[14] C.Z. Wei, W.H. Liu, Q.Y. Chen, H.Y. Hou, R. Liu, C. Cheng, C.T. Hou, W.W. Xiong, D.J. Zhang, Nitrogen-Doped ZnO/Carbon Hollow Rhombic Dodecahedral for Photoelectrochemical Sensing Glutathione, vol. 458, (2018), pp. 872–879.

[15] G. Gao, Q.Y. Xi, H. Zhou, Y.X. Zhao, C.Q. Wu, L.D. Wang, P.R. Guo, J.W. Xu, Selectivity of quantum dot sensitized ZnO nanotube arrays for improved photocatalytic activity, Phys. Chem. Chem. Phys. 19 (2017) 11366–11372.

[16] M.M. Hossain, B.-C. Ku, J.R. Hahn, Synthesis of an efficient white-light photocatalyst composite of graphene and ZnO nanoparticles: application to methylene blue dye decomposition, Appl. Sur. Sci. 354 (2015) 55–65.

[17] M.J. Sampaio, R.R. Bacsa, A. Benyounes, R. Axet, P. Serp, C.G. Silva, A.M.T. Silva, J.L. Faria, Synergistic effect between carbon nanomaterials and ZnO for photocatalytic water decontamination, J. Catal. 331 (2015) 172–180.

[18] F.-X. Xiao, J.W. Miao, H.B. Tao, S.-F. Hung, H.-Y. Wang, H.B. Yang, J.Z. Chen, R. Chen, B. Liu, One-dimensional hybrid nanostructures for heterogeneous photocatalysis and photoelectrocatalysis, Small 11 (18) (2015) 2115–2131.

[19] D. Chaudhary, S. Singh, V.D. Vankar, N. Khare, ZnO nanoparticles decorated multiwalled carbon nanotubes for enhanced photocatalytic and photoelectrochemical water splitting, J. Photochem. Photobiol. A Chem. 351 (2018) 154–161.

[20] C. Han, M.-Q. Yang, B. Weng, Y.-J. Xu, Improving the photocatalytic activity and anti-photocorrosion of semiconductor ZnO by coupling with versatile carbon, Phys. Chem. Chem. Phys. 16 (2014) 16891–16903.

[21] Y.G. Peng, J.L. Ji, D.J. Chen, Ultrasound assisted synthesis of ZnO/reduced graphene oxide composites with enhanced photocatalytic activity and anti-photocorrosion, Appl. Surf. Sci. 356 (2015) 762–768.

[22] Camilo Zamora-Ledezma, C. Blanc, Nicolas Puech, Maryse Maugey, C'ecile Zakri, Eric Anglaret, Philippe Poulin, Conductivity anisotropy of assembled and oriented carbon nanotubes, Phys. Rev. E 84 (2011) 062701.

[23] Y. Xing, L. Li, C.C. Chusuei, R.V. Hull, Sonochemical oxidation of multiwalled carbon nanotubes, Langmuir 21 (2005) 4185–4190.

[24] Q. Li, B.D. Guo, J.G. Yu, J.R. Ran, B.H. Zhang, H.J. Yan, J.R. Gong, Highly efficient visible-light-driven photocatalytic hydrogen production of CdS-cluster-decorated graphene nanosheets, J. Am. Chem. Soc. 133 (2011) 10878–10884.

[25] Y. Lei, L.Y. Gu, W.W. He, Z.X. Jia, X.G. Yang, H.M. Jia, Z. Zheng, Intrinsic charge carrier dynamics and device stability of perovskite/ZnO mesostructured solar cells in moisture, J. Mater. Chem. A 4 (2016) 5474–5481.

[26] X.Q. Zhang, Y.Y. Feng, S.D. Tang, W. Feng, Preparation of a graphene oxide-phthalocyanine hybrid through strong p-p interactions, Carbon 48 (2010) 211–216.

[27] R. Paul, R.N. Gayen, S. Biswas, S. Venkataprasad Bhat, R. Bhunia, Enhanced UV detection by transparent graphene oxide/ZnO composite thin films, RSC Adv. 6 (2016) 61661–61672.

[28] H. Moussa, E. Girot, K. Mozet, H. Alem, G. Medjahdi, R. Schneider, ZnO rods/reduced graphene oxide composites prepared via a solvothermal reaction for efficient sunlight-driven photocatalysis, Appl. Catal. B Environ. 185 (2016) 11–21.

[29] W.W. Tie, S.S. Bhattacharyya, Y.N. Wang, W.W. He, S.H. Lee, Facile in-situ synthesis of a zinc oxide crystals/few-layered graphene flake composite for enhanced photocatalytic performance, J. Photochem. Photobio. A: Chemistry 348 (2017) 89–95.

[30] M.M. Hossain, B.-C. Ku, J.R. Hahn, Synthesis of an efficient white-light photocatalyst composite of graphene and ZnO nanoparticles: application to methylene blue dye decomposition, Appl. Surf. Sci. 354 (2015) 55–65.

[31] N. Song, H.Q. Fan, H.L. Tian, Reduced graphene oxide/ZnO nanohybrids: metallic Zn powder induced one-step synthesis for enhanced photocurrent and photocatalytic response, Appl. Surf. Sci. 353 (2015) 580–587.

[32] Z.K. Cui, H.T. Song, S.X. Ge, W.W. He, Y.W. Liu, Fabrication of BiOCl/BiOBr hybrid nanosheets with enhanced superoxide radical dominating visible light driven photocatalytic activity, Appl. Surf. Sci. 467-468 (2019) 505–513.

[33] J.G. Ok, J.Y. Lee, H.W. Baac, S.H. Tawfick, L.J. Guo, A.J. Hart, Rapid anisotropic photoconductive response of ZnO-coated aligned carbon nanotube sheets, ACS Appl. Mater. Interfaces 6 (2014) 874–881.

[34] T.F. Jiang, T.F. Xie, Y. Zhang, L.P. Chen, L.L. Peng, H.Y. Li, D.J. Wang, Photoinduced charge transfer in ZnO/Cu2O heterostructure films studied by surface photovoltage technique, Phys. Chem. Chem. Phys. 12 (2010) 15476–15481.

[35] B. Li, H. Cao, ZnO@graphene composite with enhanced performance for the removal of dye from water, J. Mater. Chem. 21 (2011) 3346–3349.